MODELING CHANGES IN CLOUD STRUCTURE USING MOTION IMAGERY

H. Theiss [a*], T. Johanesen [b]

[a] Integrity Applications Incorporated, 5180 Parkstone Dr., Chantilly, VA, 20151, USA
henry.j.theiss.ctr@nga.mil
[b] National Geospatial-Intelligence Agency, 12310 Sunrise Valley Dr., Reston, VA, 20191, USA
todd.e.johanesen@nga.mil

KEY WORDS: motion imagery, sequence, surface reconstruction, direct georeferencing

ABSTRACT:

Today's GIS, imagery exploitation applications, and modelling and simulation tools could become more realistic by implementing algorithms capable of precise photogrammetric reconstruction of the 3D structure of obscurants, such as clouds or smoke. As examples, environmental engineers may require such information to determine how a plume of smoke from a factory spreads and moves over time and how that affects local wildlife and people in the area; flight simulators could become more representative of the real world by using realistic cloud modelling to train pilots; and weather forecasters could use more accurate cloud formation models, thus improving their predictions. This paper explores such modelling enhancement by using concepts found in direct georeferencing techniques, employing combinations of airborne digital frame imagery and motion imagery, to generate 3D models of clouds. The paper describes an eleven image block of low-oblique images taken from a helicopter over an ocean background. Two ships of known location are visible in each image along with a cloud emanating from one of them. A procedure is given to perform a block triangulation using time-dependent tie points, with primary purpose of initializing the values of the camera parameters. These results are then used as input to a 3D spline cloud reconstruction technique. Since the solution lacks geometric strength in the vertical direction, a height constrained solution is provided based on assumptions about the typical cloud shape. Then, a set of eleven high-oblique frames from a short motion imagery sequence is introduced which constrain the cloud height due to its large convergence angle with the low-oblique frames. Two solutions, simultaneous and sequential, are provided that use all available images to reconstruct the cloud. The paper provides tabular results of image space residuals, both overall and by image, for all techniques described. Recommendations are provided that would encourage new guidelines for image acquisition and image support data in subsequent collects. Finally, ideas for future research are provided including a plan to build a cloud simulation software tool.

1. INTRODUCTION

1.1 Purpose

The desire to recreate accurate three dimensional models of smoke, clouds and other cloud-type obscurants is well documented in today's literature. Research has shown that the generation of these models, especially the determination of cloud heights, help scientists understand how meteorology affects the world around us—from the earth's climate system, especially as it pertains to the structure and dynamics of hurricanes and severe thunderstorms (Hasler, et al, 1991) and (Moroney, et al, 2002), to the understanding of tactics and calculations for laying smokescreens, especially as it relates to the size and behaviour of such obscurants (Lavarre, 2006). In order to understand these environments, scientists build models from imagery that captures cloud height, width and overlap, along with other relevant information such as emissivity and temperature. The collected imagery supporting model development has followed traditional photogrammetric paths and has primarily focused on stereo image collection and image matching. In fact, stereoscopy of clouds has a long tradition in meteorology, primarily because a user can obtain observations of cloud features from at least two different angles (Seiz, et al, 2006). The imagery collected is based on stereo techniques and in order to be successful with image correlation, the cloud images must have sufficient contrast to support pattern matching. The full correlated stereo-pair provides scientists the necessary information and measurements for cloud motion and height determination. However, the image matching algorithms supporting the cloud-matching is not without limitations. Most of the image matching algorithms require heavy computation time due to the vast quantities of data being processed (Moroney, et al, 2002). The primary errors are a result of cloud movement, resolution, and artefacts introduced by ground objects (Poli, et al, 2000).

Starting in the 1990's, direct georeferencing techniques and multi-sensor integration developed into what is now commonly referred to as mobile mapping technology (MMT) (Tao, et al, 2004). The impetus for this development was to support real-time environmental monitoring and digital data processing to a variety of disciplines; the resulting technology supports a multitude of processes within the geoscienes community including co-registration, mapping and object location. These systems are made possible through the integration of digital imaging devices and robust navigation solutions such as those found in navigation and positioning sensors, i.e. GPS and IMUs. With rigorous time-synchronization of support data from these sensors, improved quality spatial data and objects found in the collected imagery can now be measured and mapped in a short turnaround time (Grejner-Brzezinska, 2002), just like traditional stereo-collected imagery.

In order to understand how this technology could be applied to meteorology, we applied the concepts from MMT and

synthetically generated surface-borne clouds using a cloud generator over a water-body surface. Through the objects and obscurants measured in the captured imagery, we contribute to the refinement of cloud-height and smoke-based obscurant models currently used in today's image exploitation tools.

Images of the cloud were obtained from two sources: a digital still-frame camera on a helicopter flying above and up-wind of the cloud acquiring low-oblique imagery, and a side-looking motion imagery camera on an aircraft flying cross-wind to the cloud acquiring high-oblique imagery. The cameras in the mobile mapping system consisted of visible, IR and near-IR camera systems, and using the sequence of images from these systems, the deformations and motions of the clouds were modelled over time.

Typical accuracy goals reported for cloud-height measurement after least squares adjustment is reported in the literature to be 100-500 m (Moroney, et al, 2002) , (Poli, et al, 2000) and (Seiz, et al, 2006), although more accurate geolocation can be achieved under certain constrained stereo collects.

1.2 Overview of Methodology for this paper

Following this introduction section, the paper describes the photgrammetric techniques used to triangulate the available imagery. At a high level, the strategy consists of recovering the values of camera exterior orientation using tie points using a block adjustment, and then using these recovered values along with feature observations to reconstruct the cloud in three dimensions. Section 2 describes the recovery of image exterior orientation for 11 high oblique still digital frame images acquired from a helicopter. Section 3 describes techniques for 3D cloud reconstruction, namely a spline based modelling presented in Subsection 3.1. A creative technique is presented in Subsection 3.2 to constrain the spline to realistic values in the vertical direction. Then, Subsection 3.3 describes a set of high oblique motion imagery that later became available for exploitation, and presented results of its triangulation. Subsection 3.4 provides two techniques, a sequential and then a simultaneous solution, that can use the high oblique imagery to improve the 3D reconstruction capability of the low oblique imagery. Finally, Section 4 provides conclusions, recommendations for future cloud collections, and plans for future research.

2. RECOVERY OF IMAGE EXTERIOR ORIENTATION

2.1 Description of the Data Set

The data set consists of 11 digital aerial frame images acquired obliquely from a helicopter flying at an altitude of approximately 3000 meters above sea level. Each image is 1648 rows by 2464 columns and has a reported focal length and pixel size of 256 mm and 0.011 mm, respectively. The resulting fields-of-view were 6.3 and 4.2 degrees in the row and column directions, respectively. Other than the approximate flying altitude, no support data was available regarding the position and orientation of the camera. The object scene contains two ships and a cloud emanating from the nearest ship. No additional features, other than the ocean surface, appear in the imagery. Time-stamped latitude and longitude coordinates were provided by GPS for each ship, and the images were time-stamped with respect to the same Universal Coordinated Time (UTC).

To facilitate the ingest of data into the mathematical equations, raw data was transformed to relative values. For example, the UTC times for image acquisition spanned 1054 seconds, ranging from 16:04:23 to 16:21:57. An image time vector, t_i, for i = 1 through 11, was defined as the time difference in seconds with respect to the first image as follows: 0, 24, 38, 54, 62, 350, 372, 461, 520, 877, 1054. Similarly, the latitude and longitude coordinates for the ship locations were all converted to Local Space Rectangular (LSR) Cartesian coordinates in meters with the origin coinciding with the latitude and longitude of the cloud generator ship at time 0, the X axis lying in the horizontal plane and pointing in the nominal direction of the cloud emanation (opposite the nominal wind direction), the Z axis pointing up and normal to the horizontal plane, and the Y axis completing a right-handed coordinate system. See Figure 1 for Image 7 of this low oblique image sequence, and overlaid LSR coordinate system.

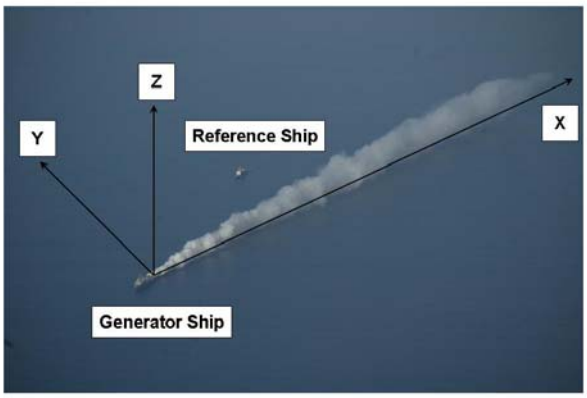

Figure 1. Image 7 – LSR System overlaid.
Image provided courtesy of US Department of Defense.

2.2 Control Features and Correlation between Them

Each image contains two control features, the two ships. The image coordinates of two points were observed on each of the two ships, one at the estimated location of the GPS receiver and the other at the top of the ship's mast. Although the approximate mast heights were provided for each ship, the 3D offset vector between the GPS receiver and top of mast is not known precisely. The ships move in approximately the same direction throughout the experiment; therefore, the uncertainty in the 3D offset vector was modelled by introducing correlations between 3D coordinates associated with each image for all four control points: 1) GPS receiver on generator ship, 2) GPS receiver on reference ship, 3) mast top on generator ship, and 4) mast top on reference ship.

The full ground coordinate covariance matrix, Σ_G is block diagonal with k = 1 through 4 sparsely filled 3n by 3n (n = number of images) covariance matrices, Σ_k, corresponding to each of the four moving control points. Associated with the i^{th} image is a diagonal 3 by 3 covariance matrix, Σ_{ki}, along the main diagonal of Σ_k populated as follows:

$$\Sigma_{k_i} = \begin{bmatrix} \sigma_{Xi}^{\ 2} & 0 & 0 \\ 0 & \sigma_{Yi}^{\ 2} & 0 \\ 0 & 0 & \sigma_{Zi}^{\ 2} \end{bmatrix} \quad (1)$$

where $\sigma_{Xi}, \sigma_{Yi}, \sigma_{Zi}$ are the variances in the *X*, *Y*, and *Z* directions expressing the precision of the control point location when it was imaged on image *i*.

Off diagonal 3 by 3 sub-blocks of Σ_k are populated with matrices expressing the correlation between the i^{th} and j^{th} images for the k^{th} control point as follows:

$$\Sigma_{k_{i,j}} = \rho \begin{bmatrix} \sqrt{\sigma_{Xi}^{\ 2}\sigma_{Xj}^{\ 2}} & 0 & 0 \\ 0 & \sqrt{\sigma_{Yi}^{\ 2}\sigma_{Yj}^{\ 2}} & 0 \\ 0 & 0 & \sqrt{\sigma_{Zi}^{\ 2}\sigma_{Zj}^{\ 2}} \end{bmatrix} \quad (2)$$

where $\rho = 0.95$ is the correlation coefficient.

While a total of four control points were measured on each image, the close proximity of a pair of points on the same ship results in poor geometry to assist in the resection of a single image. To provide more redundancy to the solution of each image's exterior orientation values, we attempted to add tie points that would allow us to perform a bundle block adjustment as described in the next subsection.

2.3 Time-dependent Tie Points Approach

2.3.1 Mathematical Modeling: Since no stationary tie points existed in the scene, one alternate approach is to measure distinct features appearing in the clouds that can be visually correlated between different image frames. Since each image was acquired at a different time and the cloud was moving and growing in three dimensions, we modelled the 3D coordinates of the i^{th} tie point as second order functions of time, for any time, *t*, as follows:

$$\begin{bmatrix} X_{ti} \\ Y_{ti} \\ Z_{ti} \end{bmatrix} = \begin{bmatrix} X_{0i} & V_X & A_X \\ Y_{0i} & V_Y & A_Y \\ Z_{0i} & V_Z & A_Z \end{bmatrix} \begin{bmatrix} 1 \\ t \\ t^2 \end{bmatrix} \quad (3)$$

where X_{0i}, Y_{0i}, Z_{0i} = the i^{th} tie point ground coordinates at time 0,
V_X, V_Y, V_Z = the tie points' velocities, and
A_X, A_Y, A_Z = the tie points' accelerations.

The following pair of equations based on the collinearity condition was written for the image coordinates of the i^{th} tie point appearing on the j^{th} image:

$$x_{ij} = -f \frac{m_{11}(X_{ti} - X_L) + m_{12}(Y_{ti} - Y_L) + m_{13}(Z_{ti} - Z_L)}{m_{31}(X_{ti} - X_L) + m_{32}(Y_{ti} - Y_L) + m_{33}(Z_{ti} - Z_L)}$$
$$y_{ij} = -f \frac{m_{21}(X_{ti} - X_L) + m_{22}(Y_{ti} - Y_L) + m_{23}(Z_{ti} - Z_L)}{m_{31}(X_{ti} - X_L) + m_{32}(Y_{ti} - Y_L) + m_{33}(Z_{ti} - Z_L)} \quad (4)$$

where f = focal length in mm,
x_{ij}, y_{ij} = image coordinates in mm,
X_{ti}, Y_{ti}, Z_{ti} = tie point coordinates, Equation (3),
X_L, Y_L, Z_L = coordinates of projection center, j^{th} image, and
$m_{pq,\ (p=1:3,\ q=1:3)}$ = 9 elements of an orthogonal rotation matrix that rotates from ground to j^{th} image coordinate system.

A pair of condition equations, i.e. Equation (4), was written for 94 image tie points and 44 image control feature points, yielding 276 total equations. The linearized form of the system of equations was $v + B\Delta = f$. A unified least squares solution was solved to recover the values of the six exterior orientation camera parameters per image. Additional unknown parameters in the adjustment included the three tie point coordinates associated with time 0, for each of the 15 ground tie points, and the six time-dependent elements describing the motion of all tie points collectively, i.e. the three velocity and three acceleration parameters defined in Equation (3). All parameters were assigned essentially zero weight since their initial values had been merely reasonable guesses. The exception, however, was that the control points were assigned weight equal to the inverse of Σ_G, which was defined in Section 2.2. See (Mikhail, 1976) as a reference for the unified least squares adjustment.

2.3.2 Weighting of Observations: The unified least squares adjustment treated all *x* and *y* image coordinates as observations. Conventional bundle adjustment procedures assign a weight matrix that assumes a diagonal covariance matrix of the observations in which: *x* and *y* image coordinates for a given point are uncorrelated with each other; and the (*x*,*y*) image coordinate pair for a given point is uncorrelated with all other image coordinate pairs in the adjustment. We first ran our adjustment using a diagonal covariance matrix, and experienced unrealistically large residuals on the observations corresponding to the control feature image points. The magnitude of the *a posteriori* reference variance was also quite large, indicating that the math model is inconsistent with the data.

To accommodate the fact that the time-dependent tie points do not adequately fit the Equations (3), we attempted to model the uncertainty in the cloud model as a 2 by 2 image space covariance matrix associated with each imaged time-dependent tie point. The error ellipse associated with such a covariance matrix would have essentially the same orientation of the cloud which is shaped similar to an ellipse in each image; see Figure 2. Our strategy for each image was to measure the image space length and width of the cloud and use these to estimate the semi-major and semi-minor axes of an error ellipse, i.e. *a* and *b*, respectively. Following is the equation of the 2 by 2 image covariance matrix associated with each point on a given image:

$$\underset{2,2}{\Sigma} = kEDE^T \quad (5)$$

where $D = \begin{bmatrix} a^2 & 0 \\ 0 & b^2 \end{bmatrix}$, $E = \begin{bmatrix} e_x & -e_y \\ e_y & e_x \end{bmatrix}$,

e_x, e_y = elements of the normalized eigenvectors associated with the error ellipse, and

k = a common scale factor applicable to all images.

A value of 0.2 was chosen for the scale factor, k, which implies that due to the inadequacy of the math model to fit the data the imaged locations of the time-dependent tie points have a precision of approximately one fifth of the cloud extent.

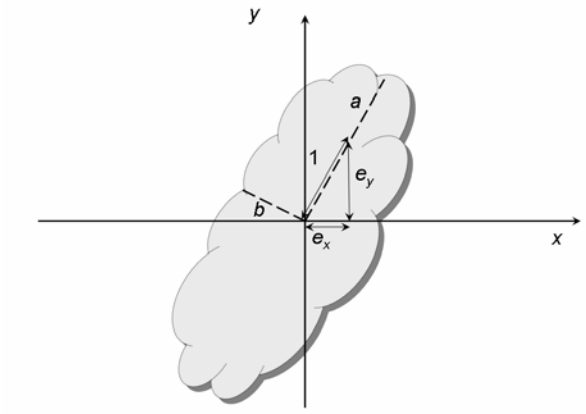

Figure 2. Image space extent of a cloud

2.3.3 Triangulation Results: The Root Mean Square (RMS) of image coordinate residuals, converted from mm to pixels for convenience, are provided in Table 1, including: all points on all images, control points, tie points, and by-image. For each line in the table, three RMS values are provided corresponding to RMS of *x* residuals, RMS of *y* residuals, and RMS of all (*x* and *y*) residuals. The magnitude of the *a posteriori* reference variance was 3.5.

While the magnitude of these RMS values are too large to have confidence in the 3D reconstruction capabilities, our intent is to use the recovered values for all images' exterior orientation and associated covariance matrix as initial approximations to the next step of reconstructing the cloud in 3D. While these residuals are large in magnitude, the residual vectors are generally oriented in the lengthwise direction of the cloud as per Equation (5); hence we obtained a fairly reasonable *a posteriori* reference variance. Furthermore, the resolution of these still frames is relatively large, equating to a large ground sample distance; thus larger residuals are expected.

	RMS v_x	RMS v_y	RMS v
All points	179.1	128.6	155.9
Control points	0.6	1.3	1.0
Tie points	179.3	134.3	158.4
Image 1	97.7	60.8	81.4
Image 2	17.6	29.1	24.1
Image 3	23.0	40.7	33.1
Image 4	23.3	39.2	32.2
Image 5	13.1	15.3	14.3
Image 6	274.5	123.6	212.9
Image 7	296.3	155.9	236.8
Image 8	91.4	144.3	120.8
Image 9	61.8	181.0	135.3
Image 10	409.3	323.3	368.8
Image 11	293.8	120.7	224.6

Table 1. Residual RMS in pixels for tie point technique

3. RECONSTRUCTION OF CLOUD IN 3D

As discussed in Section 2, the time-dependent tie point method is an inadequate technique to support reliable 3D reconstruction. However, the triangulation results provide reasonable estimates for the camera exterior orientation parameters and associated uncertainty. This section provides a mathematical formulation for modelling the cloud in 3D. Then, due to the relatively weak geometry of the images, constraints on the vertical dimension of the clouds are imposed based on the behaviour of clouds in their current weather conditions. Finally, an attempt is made to independently verify the cloud dimensions recovered using this technique.

3.1 Mathematical Modeling of 3D Spline

The cloud observed in this experiment began at the rear end of the generator ship, which moved towards the wind (-X direction), and extended in the downwind direction (+X direction). The cloud structure remained continuous throughout the imaging sequence. The cloud became relatively elongated over time with the length, essentially the X direction, always significantly larger than its width, essentially Y, or height, Z. Since the ship moved at approximately the same rate throughout the duration of the experiment and the wind speed remained relatively constant, the cloud growth was modelled as a linear function of time. The cloud shape was modelled as a time-varying 3D spline of fourth order in the X, Y, and Z directions as follows:

$$\begin{aligned} X_t &= X_{0t} + (1 + S_X t)(a_1 u + a_2 u^2 + a_3 u^3 + a_4 u^4) \\ Y_t &= Y_{0t} + (1 + S_Y t)(b_1 u + b_2 u^2 + b_3 u^3 + b_4 u^4) \\ Z_t &= Z_{0t} + (1 + S_Z t)(c_1 u + c_2 u^2 + c_3 u^3 + c_4 u^4) \end{aligned} \quad (6)$$

where X_{0t}, Y_{0t}, Z_{0t} are the known coordinates of the beginning of the spline at time t,

a_j, b_j, $c_{j\ (j=1:4)}$ = shape coefficients of the spline,

S_X, S_Y, S_Z = growth rate coefficients of the spline, and

u = unitless location along spline ranging from 0 to 1.

Approximately six to ten image points were observed per image along the perceived centreline of the cloud from its beginning to end. As in the case for the time-dependent tie point triangulation, a pair of condition equations, i.e., Equation (4), was written for each image point. A total of 174 equations were written, two per point for 87 spline points. The unknowns consisted of three parts: 1) The 66 camera exterior orientation parameters; 2) the 15 spline coefficients appearing in Equation (6); and 87 u values for each image point observation which were estimated as the ratio of its image space distance (with respect to the beginning) to the total image space cloud length. A unified least squares solution was solved to recover the values of all unknown parameters. The *a priori* weight matrix for the 66 exterior orientation parameters was assigned values corresponding to the inverse of the covariance matrix described

in Section 2.3.3. The values of the *a priori* weight matrix for the 15 spline coefficients was zeroes, while the *u* parameters had to be assigned relatively large weights in the adjustment.

The covariance matrix of the observations was constructed as a diagonal matrix with variances of 0.25 pixels squared along the diagonal. The RMS values of image coordinate residuals, converted from mm to pixels for convenience, are provided in Table 2, including: all points on all images, and by-image. The magnitude of the *a posteriori* reference variance was 325.

	RMS v_x	RMS v_y	RMS v
All points	5.9	3.5	4.8
Image 1	4.2	4.8	4.5
Image 2	1.0	2.6	2.0
Image 3	10.3	3.5	7.7
Image 4	7.9	2.8	5.9
Image 5	6.0	1.7	4.4
Image 6	3.5	3.5	3.5
Image 7	3.0	2.5	2.8
Image 8	3.2	1.7	2.6
Image 9	8.6	2.7	6.4
Image 10	7.7	5.7	6.7
Image 11	2.5	3.2	2.9

Table 2. Residual RMS in pixels for spline technique

Notice how drastically the magnitudes of the RMS residuals were reduced by using the 3D spline technique instead of time-dependent tie points; compare Tables 1 and 2. Unfortunately, however, the values of the reconstructed cloud heights are not reasonable. For example the centreline height of the cloud end was computed by evaluating the spline equations for the first, seventh, and last images in the sequence, yielding values of -54 meters, +2426 meters, and +6973 meters, respectively. Of course we know that the height must be positive at both times and will likely increase as a function of time. Following sections will attempt to constrain the cloud height.

3.2 Cloud Height Constraints

3.2.1 Cloud Behaviour in Stable Air: A recent paper on nomograph regressions (LaVarre, 2006) provides the results of fitting mathematical regression equations as a substitute to the nomographs that had been developed in the 1940s. Nomographs provide a graphical means of calculating cloud heights, widths, and lengths as a function of wind speed and air stability. The air was considered stable on the day of this experiment which means that the air near the surface of the earth (ocean in our case) is colder than the air above it. The cloud remained stable because heat has a tendency to rise, and therefore the cooler air at the ocean surface did not try to force its way upward into the warmer air. So the cloud in our experiment stretched out in the wind direction, but the base of the cloud remained essentially at the ocean surface. The surface of the cloud itself remained relatively smooth and continuous.

3.2.2 Implementation of Cloud Height Constraints: As mentioned in Section 3.1, the 3D reconstruction geometry was weak in the vertical direction and, as demonstrated by the results, unreasonable cloud heights were calculated. Ideally we would use high oblique images looking almost horizontally parallel to the ground space LSR Y axis, such that the X and Z LSR axes point towards the right and upward, respectively, in the image space. In the absence of such high oblique images, the next best alternative was to constrain the cloud heights to reasonable values.

Visual inspection of the cloud images revealed that, in addition to the base of the cloud remaining at the ocean surface, the cloud height appeared to be approximately equal to the cloud width throughout the length of the cloud; i.e., the cloud cross-section approximated a circle. Therefore, our strategy was to measure the edges of the cloud at each of the six to ten points per image where we measured the centreline of the spline, as discussed in Section 3.1. Using the adjusted camera exterior orientation support data from the 3D reconstruction adjustment described in Section 3.1, we computed the ground space 3D coordinates of each edge of the cloud at a position *u* along the spline in image *j*. Then we computed the cloud width as the spatial distance between these two edge points. Recall that the spline mathematically represents the perceived centreline of the cloud. So, if the base of the cloud is at the ocean surface and the height of the cloud equals its width, then the spline height will equal half of the cloud height, or equivalently half of the cloud width.

For each image and for each position *u* along the spline in that image, a condition equation was written for the Z (third) of Equation (6). For each of these equations, the Z value was set equal to half the cloud width, as discussed in the previous paragraph. A least squares adjustment was then solved to determine the five coefficients of the spline Z equation; call this Step 1. Then a 3D object reconstruction adjustment was run as described in Section 3.1, but this time holding the Z coefficients of the spline as fixed; call this Step 2. The cloud height constrained 3D reconstruction adjustment consisted of an outer iterative loop that repeated Steps 1 and 2 until the least squares adjustment residuals of Step 2 remained essentially the same between successive outer-loop iterations.

The RMS of image coordinate residuals, converted from mm to pixels for convenience, are provided in Table 3, including: all points on all images, and by-image. The magnitude of the *a posteriori* reference variance was 100.

	RMS v_x	RMS v_y	RMS v
All points	4.5	3.6	4.1
Image 1	2.4	3.7	3.1
Image 2	1.9	1.1	1.5
Image 3	6.1	1.4	4.4
Image 4	4.3	1.5	3.2
Image 5	3.9	2.6	3.3
Image 6	1.8	4.1	3.2
Image 7	2.7	4.7	3.8
Image 8	4.0	1.9	3.1
Image 9	10.4	5.7	8.3
Image 10	3.0	3.0	3.0
Image 11	2.0	5.0	3.8

Table 3. Residual RMS in pixels for the height constrained spline technique

Notice how in the case of the height constrained spline technique the magnitudes of the RMS residuals remained relatively small as in the unconstrained 3D spline technique; compare Tables 2 and 3. Also the *a posteriori* reference variance decreased after imposing the constraints. These results show that by imposing realistic constraints, the observations still fit the model as well or better than without the constraints. Again, the centreline height was computed at the cloud ends for times corresponding to images 1, 7, and 11, yielding values of +135 meters, +203 meters, and +328 meters, respectively. Since these heights correspond to the centreline of the cloud, the heights of the top of the cloud would be double the heights calculated by the spline.

3.3 Triangulating High Oblique Imagery

Subsections 3.1 and 3.2 described the difficulties in recovering the cloud height dimension, and offered creative methods to constrain the solution to achieve more reasonable coordinates. After implementing these constrained solutions, the authors later received a video stream containing high oblique frames taken essentially parallel to the LSR Y axis. Section 2.1 listed the times ranging from 0 to 1054 seconds, corresponding to the first and last images of the low oblique still frame images. The high oblique motion imagery sequence was acquired over a short 13 second period between image 6 and image 7 of the low oblique sequence. Eleven high oblique frame images were saved from the motion imagery sequence. This is coincidently the same number of still frame images that were used in the previous subsections. Figure 3 illustrates the time of acquisition corresponding to each image frame.

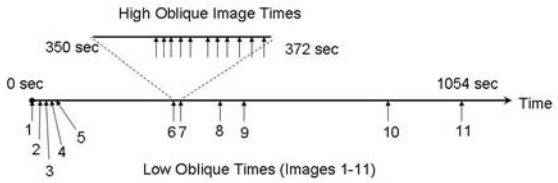

Figure 3. Image times

The authors received a short video clip of imagery taken from a tripod aimed directly forward at a square of known dimensions drawn on a whiteboard. The 240 (rows) by 320 (columns) pixel image was acquired at a known distance from the whiteboard. Using the measured image coordinates of the four corners of the square, a single image resection was solved for the five exterior orientation parameters (range component of perspective center was held fixed) and focal length; i.e., the solution consisted of eight condition equations and six unknown parameters yielding a redundancy of two. A focal length value of 3346.0 pixels was recovered, corresponding to 4.1 and 5.5 degree fields-of-view in the row and column directions, respectively.

During the 13 second image acquisition of the cloud, the video camera was onboard an aircraft travelling in approximately the positive LSR Y direction. Therefore, had the field-of-view been sufficiently wide, the cloud generator ship would have appeared on the left side of each image and the cloud would emanate from this ship growing taller towards the right. The camera was capable of slewing in the azimuth and elevation directions with respect to the aircraft platform. Zero azimuth and zero elevation angles would point in the direction of the nose of the aircraft, i.e. in the direction of the velocity vector. The elevation angle remained approximately constant at an angle of -1.0 degree (one degree down from the velocity vector). The azimuth angle began at -9.9 degrees (Image 1), moved positive (clockwise, or towards the right) to +1.3 degrees (Image 6), and then slewed back towards the left, finishing at an azimuth of -13.6 degrees (Image 11).

We proceeded to measure the necessary image coordinates on these 11 high oblique images that would allow us to perform a block adjustment to solve for all of the 66 camera exterior orientation parameters. Control points consisted of the front and rear points of the cloud generator ship, which appeared only on Images 1 and 11. Unfortunately, from a geopositioning standpoint, the reference ship remained obscured in all 11 images. The front and rear points of the ship were treated as four separate control points, since their values changed during the 13 seconds between Images 1 and 11. Ten distinct tie points, approximately evenly spaced in the LSR X direction, could be observed on the top surface of the cloud in two or more images per point. Ten vertical control points, corresponding to each tie point, were observed directly below the associated tie point precisely where the cloud meets the water.

As in the case for the time-dependent tie point triangulation, a pair of condition equations, i.e., Equation (4), was written for each image point yielding a total of 164 condition equations. The unknowns consisted of four parts: 1) The 66 camera exterior orientation parameters; 2) the 60 ground coordinate parameters for the 10 tie points and 10 vertical control points; and 3) the 12 ground coordinate parameters for the four control points; and 4) one parameter for the velocity of the tie points in the X direction as per Equation (3). Velocities in other directions and accelerations were considered negligible over this short time duration. A unified least squares solution with constraints was solved to recover the values of all unknown parameters. Due to the sparse control, poor point distribution, and poor convergent geometry, we used constraint equations instead of assigning arbitrarily large weights to the parameters in order to perform the block adjustment. Our first set of constraints was among the exterior orientation parameters. We assumed a straight line aircraft trajectory, and thus wrote three constraint equations for each of Images 2 through 10, yielding 27 constraint equations. Our second set of constraints was among the tie and vertical control points. We wrote 20 constraint equations that constrained the X and Y ground coordinates to be equal between each tie point and its corresponding vertical control point. The final set of constraints was to constrain the distance between the front and rear of the ship to equal the known ship length. Two constraint equations of this type were written, corresponding to the times of the first and last images.

The linearized form of the system of condition equations and constraint equations was $v + B\Delta = f$ and $C\Delta = g$, respectively. The covariance matrix of the image coordinate observations was constructed as a diagonal matrix with variances of 2.25 pixels squared along the diagonal. The RMS values of image coordinate residuals, in pixels, are provided in Table 4, including: all points on all images, and by-image. The magnitude of the *a posteriori* reference variance was 1.0. Error propagation yielded one sigma uncertainties in the cloud height ranging from 3 meters to 13 meters at points nearest to and farthest from the cloud generator ship, respectively.

	RMS v_x	RMS v_y	RMS v
All points	1.2	0.9	1.1
Image 1	1.5	1.1	1.3
Image 2	1.0	1.4	1.2
Image 3	1.1	0.6	0.9
Image 4	2.2	1.0	1.7
Image 5	0.7	0.3	0.5
Image 6	0.9	0.3	0.7
Image 7	0.4	0.5	0.4
Image 8	0.6	0.8	0.7
Image 9	0.8	0.7	0.8
Image 10	1.2	0.7	1.0
Image 11	1.8	1.3	1.5

Table 4. Residual RMS in pixels for the high oblique motion image frames

3.4 Combining All Imagery Sources

Subsections 3.1 and 3.2 used low oblique imagery in an attempt to reconstruct the cloud, while Subsection 3.3 used high oblique imagery. We will now proceed with two methods to incorporate strong geometry in the Z direction provided by the high oblique imagery to improve the accuracy of the low oblique imagery.

3.4.1 Simultaneous Solution: This solution consisted of a reconstruction of the 3D spline representation of the cloud using all 22 image, 11 low oblique and 11 high oblique. The mechanics for this 22 image block adjustment were identical to that described in Subsection 3.1. The *a priori* covariance matrix for the 132 exterior orientation parameters was a block diagonal matrix consisting of two 66 by 66 full covariance matrices for the low oblique and high oblique images; these were derived from the inverse of the normal equations matrices of the block adjustments described in Subsections 2.3.3 and 3.3, respectively. The RMS values of image coordinate residuals, converted from mm to pixels for convenience, are provided in Table 5, including: all points on all images, and by-image. The magnitude of the *a posteriori* reference variance was 3.5.

	RMS v_x	RMS v_y	RMS v
All points	7.3	4.7	6.1
Image 1	12.0	7.2	9.9
Image 2	4.5	2.9	3.8
Image 3	12.8	0.7	9.1
Image 4	6.5	2.3	4.9
Image 5	4.3	2.7	3.6
Image 6	5.0	6.4	5.7
Image 7	4.1	4.4	4.3
Image 8	3.9	2.9	3.4
Image 9	10.9	3.0	8.0
Image 10	12.6	7.2	10.3
Image 11	8.4	7.1	7.8
Image 12	2.0	1.8	1.9
Image 13	1.5	1.2	1.3
Image 14	0.9	1.4	1.2
Image 15	0.7	4.0	2.9
Image 16	3.0	5.1	4.2
Image 17	4.8	10.2	8.0
Image 18	3.7	4.1	3.9
Image 19	3.4	3.7	3.6
Image 20	3.7	3.7	3.7
Image 21	3.7	3.3	3.5
Image 22	4.3	3.6	3.9

Table 5. Residual RMS in pixels for the low oblique (Images 1-11) and high oblique (Images 12-22) imagery

3.4.2 Sequential Solution: This solution used the results of the triangulation described in Subsection 3.3 to fit the Z component of the 3D spline. The recovered Z values for each of the 10 tie points, used in the high oblique block adjustment, were used to generate a system of 10 equations with four unknowns (c_1, c_2, c_3, c_4), using the third of Equation (6). Then, the adjusted values of these four parameters and associated four by four covariance matrix were entered into a block adjustment essentially the same as that described in Subsection 3.2. The only difference is that, instead of the cloud height constraint being based on the cloud width, the cloud height was fixed to the heights as defined by the four aforementioned coefficients (c_1, c_2, c_3, c_4). These coefficients were not refined in the solution; therefore, the outer iteration loop described in Subsection 3.3 was not used in this solution. The RMS values of image coordinate residuals, converted from mm to pixels for convenience, are provided in Table 6, including: all points on all images, and by-image. The magnitude of the *a posteriori* reference variance was 247.

	RMS v_x	RMS v_y	RMS v
All points	6.2	5.6	5.9
Image 1	5.4	6.9	6.2
Image 2	1.1	1.6	1.4
Image 3	12.3	2.8	8.9
Image 4	9.0	6.1	7.7
Image 5	5.0	3.0	4.1
Image 6	5.0	9.5	7.6
Image 7	4.7	8.1	6.7
Image 8	4.3	2.1	3.4
Image 9	6.8	2.9	5.2
Image 10	6.5	6.0	6.2
Image 11	1.6	3.0	2.4

Table 6. Residual RMS in pixels for the sequential, high oblique followed by low oblique, solution

4. CONCLUSIONS AND FUTURE RESEARCH

4.1 Conclusions

This paper provided novel approaches to 3D cloud reconstruction from sequences of low oblique imagery taken

from the same platform with relatively poor convergent geometry and no observed values for exterior orientation. Then the paper attempted to improve the accuracy of the 3D reconstruction when high oblique motion imagery became available for relatively short 13 second duration of time.

The real data results confirmed the authors' suspicions about accurately recovering 3D cloud data from such imagery, and reinforced the claim that simultaneous image acquisition from at least two platforms with relatively widely varying view angles is necessary to improve 3D reconstruction accuracy. We recommend the following additional actions for any subsequent collections: 1) perform a more sophisticated camera calibration prior to the actual cloud collection to obtain an accurate focal length estimate and potentially recover other interior orientation values; 2) attempt to acquire observations for all images' exterior orientation elements including both position and attitude data as a function of time, e.g. using GPS and an inertial measurement unit (IMU) onboard the platform; 3) place more control points, e.g., ships equipped with GPS data, in the scene; and 4) place stationary tie points such as anchored buoys widely spread throughout the ground scene.

4.2 Future Research

The authors hope to continue this research by participating in the planning, as well as photogrammetric reduction, of additional image collects of cloud scenes. We plan to investigate using automated tools to correlate tie points on the surface of the cloud, as is performed in typical DEM generation scenarios. Then, we will investigate surface representation techniques that accurately reconstruct the 3D surface of the cloud. Further efforts will provide more detailed error propagation results to accompany the 3D cloud data. Finally, we anticipate eventually implementing our concepts for visualization of 3D clouds that will allow a user to enter a flight trajectory that initiates a fly through illustrating which object features are obstructed by the cloud, and when.

ACKNOWLEDGMENTS

The authors acknowledge the US DoD for their financial support of this research, contract number HM1582-06-C-0014. Specifically, the authors acknowledge Mr. C. Andrews LaVarre with sincere thanks for providing extensive technical support throughout the project.

REFERENCES

Grejner-Brzezinska, D., 2002. Direct Georeferencing at The Ohio State University: A Historical Perspective. *Photogrammetric Engineering and Remote Sensing*, 68(6), pp. 557-560

Hasler, A.F., Strong, J., Woodward, R.H., Pierce, H., 1991. Automatic Analysis of Stereoscopic Satellite Image Pairs for Determination of Cloud-Top Height and Structure. *Journal of Applied Metrology*, 30, pp. 257-281.

LaVarre, C. A., 2006. USF 81 Nomogram Regressions. Report, Warfare Development Command, Newport, RI, USA.

Mikhail, E.M., Bethel, J.S., McGlone, J.C., 2001. *Introduction to Modern Photogrammetry*. John Wiley and Sons, New York, NY.

Mikhail, E.M., 1976. *Observations and Least Squares*. University Press of America, New York, NY.

Moroney, C., Davies, R., Muller, J., 2002. Operational Retrieval of Cloud-Top Heights Using MISR Data. *IEEE Transactions on Geoscience and Remote Sensing*, 40(7), pp. 1532-1540.

Poli, D., Seiz, G., Baltsavias, M., 2000. Cloud-top Height Estimation from Satellite Stereopairs for Weather Forecasting and Climate Change Analysis. *International Archives of Photogrammetry and Remote Sensing*, Amsterdam, The Netherlands, Vol. XXXIII, Part B7, pp. 1162-1169.

Seiz, G., Davies, R., Grun, Armin, 2006. Stereo Cloud-Top Retreival with ASTER and MISER. *International Journal of Remote Sensing*, 27(9), pp. 1839-1853.

Tao, V., Mostafa, M., 2004. A Report on the 4th International Symposium on Mobile Mapping Technology (MMT 2004). *Photogrammetric Engineering and Remote Sensing*, 70(8), pp. 883 & 893